Applied Energy 292 (2021) 116911

Contents lists available at ScienceDirect

Applied Energy

journal homepage: www.elsevier.com/locate/apenergy

Magnetic field energy harvesting from the traction return current in rail tracks

Yang Kuang [a], Zheng Jun Chew [a], Tingwen Ruan [a], Tim Lane [b], Ben Allen [b], Bimal Nayar [b], Meiling Zhu [a,*]

[a] College of Engineering, Mathematics and Physical Sciences, University of Exeter, Exeter EX4 4QF, UK
[b] Network Rail, The Quadrant MK, Elder Gate, Milton Keynes MK9 1EN, UK

HIGHLIGHTS

- Traction return current is a promising source for railway energy harvesting.
- A magnetic core partially enclosing the rail track can increase the power output.
- The optimal design should trade effective permeability against eddy current loss.
- Nonlinear magnetization and magnetic saturation leads to increased optimal load.
- The harvester produced average power of 5.05 W under a rail current of 520 A.

ARTICLE INFO

Keywords:
Condition monitoring
Energy harvesting
Railway
Inductive coil
Eddy current

ABSTRACT

Alternating magnetic fields generated by AC traction return currents in rail tracks are an untapped energy source that can be scavenged by a magnetic field energy harvester (MFEH) to power wireless condition monitoring sensors. This paper reports the first comprehensive study on the design, optimisation and experimental testing of such MFEH. The magnetic core has been specially designed with two flux collectors partially enclosing the rail track to increase the power output. An electromagnetic-circuit coupled finite element model (FEM) has been developed to optimise the design under the influence of eddy current loss in the rail track, which has not been investigated before. The simulation reveals that an optimal design should trade off the effective permeability against the eddy current loss, instead of purely maximising the effective permeability as in previous studies. The effects of the various design parameters on the performance of the MFEH have been investigated to obtain an optimised design. An optimised design has been prototyped and tested under a section of current-carrying rail track. The experimental results showed good agreements with simulations. Experimental results show that nonlinear magnetization and magnetic saturation has negatively affected the power generation but the effect can be minimised by increasing the load resistance. The MFEH has produced average power of 5.05, 3.5 and 1.6 W, when placed at 48, 95, 190 mm from the rail track carrying 520 A at 50 Hz, respectively. The power generated has a significant potential for powering wireless sensors for a range of railway monitoring applications.

1. Introduction

Rail transport of passengers and freight are vital to the economy and society and is under rapid development, upgrading and expansion worldwide [1]. In the UK alone, there are>4, 000 trains running on 20,000 miles of rail track and transporting 1.7 billion passenger journeys and 17 billion tonne-kilometres of domestic freight [2]. One significant issue faced throughout the world is the deterioration of rail infrastructure [3], which usually causes unplanned maintenance, delays, disruption or reduction in availability, resulting in significant cost being incurred unnecessarily. It is therefore of utmost importance that the deterioration can be detected in the early stage so that the maintenance can be performed in a planned and predictive way. Traditional human inspection is conducted periodically every year or several months, which is inefficient and may not identify the faults in a timely way [3]. In contrast, condition monitoring monitors the rail

* Corresponding author.
E-mail address: m.zhu@exeter.ac.uk (M. Zhu).

https://doi.org/10.1016/j.apenergy.2021.116911
Received 8 December 2020; Received in revised form 20 February 2021; Accepted 31 March 2021
Available online 12 April 2021

infrastructure in real-time and therefore can detect the faults before they cause damage or prevent rail operation, leading to reduced maintenance and costs. Condition monitoring based on wireless sensor networks (WSNs) has attracted more and more attention, compared to its wired counterpart, because of the great flexibility and low installation cost by eliminating cabling. However, one challenge with WSN is the power source. Conventional batteries have limited capacity and lifetime. Regular replacement or recharging of the batteries is challenging for a WSN with a great number of nodes distributed in geography across the rail infrastructure. A promising solution to this challenge is energy harvesting, which converts the ambient energy source to supply the WSN [4].

In the past two decades, significant research efforts have been devoted to energy harvesting around rail tracks aiming to provide a sustainable power source for condition monitoring sensors and trackside equipment [5]. Wang *et al.* [6] developed two energy harvesters: a piezoelectric cantilever and a turbine to harvest the wind energy induced by trains passing by. Pan *et al.* [7] developed an EH with two rotors to harvest both the natural wind and the train-induced wind in a tunnel, producing 107.76 mW at a wind speed of 11 m/s. Cahill *et al.* [8] evaluated adhesive piezoelectric patches for energy harvesting from the train-induced strains in bridges. Wang *et al.* [9] evaluated both patch-type and stack-type piezoelectric transducers to harvest energy from rail tracks. Gao *et al.* [10] exploited the thermal gradient between the bottom of the rail and the soil or ballast underneath the track to generate electricity. This generated 5.8 mW with a temperature difference of 8 °C in field tests and 316.8 mW with 29.2 °C in lab tests. Since the thermal gradient fully relies on the weather conditions, so does the power output. Kroener *et al.* [11,12] proposed harvesting energy from the variable magnetic reluctance induced by the wheels passing by a magnetic circuit. The energy measured in a simulated condition was 10–40 μJ per wheel passage. The research relating to wind and thermal energy sources around rail tracks is still limited. In contrast, energy harvesting from the train-induced track deflection has been intensively studied [13–15]. The track deflection was converted to rotary motion through mechanisms such as hydraulic system [16], rack and pinions [17] and ball-screw [18], and used to drive geared rotary motor following mechanical rectification. Electric power up to a few watts could be produced, although the reliability and longevity are still in question and require further investigation.

While wind, thermal and mechanical energy harvesting around rail tracks have all been investigated, one promising energy source that has not been exploited so far is the magnetic field energy produced by the traction return current. In electrified railways, rail tracks are usually used as the returning path of traction currents. When the traction current is AC, it produces a varying magnetic field in its vicinity, which can be converted to electricity. Magnetic field energy can be converted first to mechanical energy by permanent magnets [19] or magnetostrictive materials [20] and then to electricity by a piezoelectric material. A more straightforward way with higher efficiency and power output, however, is the use of a coil to harvest the energy based on Faraday's Law, which is referred to as magnetic field energy harvester (MFEH) in this study. Compared with the energy sources and method mentioned above, the magnetic field energy is not affected by weather conditions and the MFEHs are free of issues such mechanical fatigue and longevity.

The MFEHs can be classified as cable-mounted and free-standing [21]. Cable-mounted MFEHs are wrapped around the source of the magnetic field—the current conductor [22,23]. A typical example is a toroid coil with a magnetic core enclosing the current conductor [22]. White *et al.* [23] developed a coil-based energy harvester with novel U-shaped flux guides wrapping around a power line. The energy harvester produced 1.5 W of power line current was 100 A_{rms}. when the simulated power-line Although cable-mounted MFEHs are capable of producing high power (up to a few watts) due to the high effective permeability of the magnetic core, wrapping around current conductors like rail tracks is not permitted. Unlike cable-mounted, free-standing MFEHs do not enclose the current conductor and therefore has greater flexibility of installation and application. The most common design is a solenoid wounded on a magnetic core. Because the magnetic core is open, free-standing MFEHs suffer from low effective permeability due to the demagnetization effect [24] and produce lower power than the cable-mounted. As a result, most of the studies on MFEHs have focused on optimising the shape of the magnetic core to increase the effective permeability and power output. Roscoe and Judd [21] found that a thinner and longer rod-shaped magnetic core had a higher effective permeability and could increase the power density. Compared with conventional rod-shaped core, dumbbell-shaped core, which have flanges on both ends of a rod-shaped core provides a higher effective permeability [25] and have attracted attention in recent years. Several magnetic cores based on this concept have been developed for energy harvesting and the enhanced effective permeability has shown to increase the power output. Yuan *et al.* developed a bow-tie-shaped core [24] and a helical core [26] for energy harvesting from overhead power lines. MnZn ferrite was selected as the material for the cores as it has low electrical conductivity to prevent the generation of eddy current in the core and high magnetic permeability to intensify the external magnetic field. The specially designed magnetic cores have demonstrated good capability of increasing the effective permeability and power output of the energy harvesters, though the fabrication of the complex magnetic cores out of brittle ferrite is costly and the winding of the helical core is difficult. Wright *et al.* [27] developed an MFEH with a funnel H-shaped core for energy harvesting from an H-shape current-carrying structural rail used in aircraft. The MFEH was tested around cables carrying 20 A current. A power output ~ 1 mW was produced when the frequency of the current was 800 Hz.

The free-standing MFEHs mentioned above [21,24–27] produced a power level of a few milliwatts. The power can be used for low power-consumption sensors such temperature sensors and MEMS accelerometers, but it is not sufficient to supply high power-consumption (sub-watts level) sensors such as acoustic emission sensors, strain gauges and pressure sensors, which are often used in the condition monitoring of rail tracks [1]. While these studies [21,24–27] maximized the effective permeability of the magnetic core to increase the power output, they have not considered the potential eddy current loss generated in the current conductor. As will be demonstrated in this study, when a rail track is used as the current conductor, the eddy current loss generated in the rail track can significantly affect the optimal design and performance of the MFEH. Maximising the effective permeability of the magnetic core increases the open-circuit voltage output but may also induce excessive eddy current loss, leading to reduced power output. Instead of purely maximising the effective permeability, the optimal design of the magnetic core should trade off the effective permeability against eddy current loss. The eddy current loss also affects the optimal values of the coil length and number of windings. Moreover, the free-standing MFEHs in the literature [21,24–27] were designed and tested with a focus at low magnetic field, at which the magnetic core is far from magnetic saturation. The performance of the MFEHs approaching magnetic saturation has not been thoroughly characterized.

This paper presents the first comprehensive study on the design, optimisation and experimental testing of an MFEH for current-carrying rail track. A magnetic core tailored for the current-carrying rail track was designed and optimised to maximise the power output. An electromagnetic-circuit coupled finite element model has been developed and to optimise the design. The effects of the eddy current losses on the performance of the MFEH have been investigated by the FEM and validated by experiments. An optimised MFEH was tested under a rail track carrying a current up to 520 A. The performance of the MFEH exposed to various magnetic field strengths until magnetic saturation was measured and compared with simulation. The developed MFEH can produce multi-watt-level power and therefore can power a range of high-power consumption wireless sensors.

2. Theoretical analysis

2.1. Traction return current in the rail track

Electric trains are powered by railway electrification systems. There are various electrification systems in use throughout the world. They can use either direct current (DC) or alternating current (AC) and may be different in terms of the voltage amplitude, line frequency and the contact methods [28]. One common feature of modern railway electrification systems is the use of the rail track as the return path of the traction current [29,30]. One example of such a system is schematically shown in Fig. 1(a), where the train is powered by a 25 kV AC electrification system based on auto-transformers [30]. The traction current, which is in the range from a few hundred to >1000 A, is supplied by the feed station and the auto-transformers through the contact wire. The traction current passes through the motor in the locomotive and flows to the rail track at earth potential via the rolling stock axles. The traction current then returns to the feed station through the rail track and the auxiliary feeder wire. Since the rail tracks are earthed, part of the traction current returns through the earth. The traction current in the rail track is concentrated on the surface and corners, as shown in Fig. 1 (b) due to the skin effect. This gives rise to the highest flux density around the corners of the rail head and foot, as shown in Fig. 1 (c). The varying magnetic field is an untapped energy source and can be harvested according to Faraday's law.

2.2. Energy harvesting from magnetic fields

Fig. 2 (a) shows a schematic of the MFEH developed in this study and placed in the proximity of a rail track. The MFEH features a coil and a magnetic core. The magnetic core consists of a rod and two flanges acting as flux collectors. The large surface of the flux collectors can guide magnetic flux from the air to the magnetic core and through the coil [24,31] and therefore increases the effective permeability and power generation. The MFEH is placed under the rail track so that the magnetic core partially encloses the rail track and the high-strength magnetic fields around both corners of the rail foot (see Fig. 1(c)) will be guided to the core. The design and optimisation of the magnetic core will be discussed in the later sections.

When a sinusoidal current with an amplitude of I_r and frequency ω runs in the rail track, it produces a magnetic field, which induces an electromotive force (EMF) in the coil. The EMF can be expressed according to Faraday's law as [24]

$$EMF = V_{OC} = N\omega A_e \mu_{r,e} B_{ex} = N\omega A_e B_{oc} \tag{1}$$

where $B_{ex} = \mu_0 H_{ex}$ is the average flux density generated by I_r in the middle cross-section of the magnetic rod;μ_0 is the permeability of free space; H_{ex} is the magnetic field; N the number of windings of the coil; A_e is the effective cross-section area of the coil (which is the same as the cross-section area of the magnetic rod in this case); $\mu_{r,e}$ is the effective relative permeability of the magnetic core; $B_{oc} = \mu_{r,e} B_{ex} = \mu_{r,e}\mu_0 H_{ex}$ is defined as the open-circuit flux density.

The MFEH connected to a circuit can be represented by the equivalent circuit model shown in Fig. 2 (b). R_c and L_c are the coil resistance and inductance. C is a compensating capacitor used to tune out the coil inductance [32]:

$$C = \frac{1}{\omega^2 L_c}, L_c = \frac{\mu_0 \mu_{r,e} N^2 A_e}{l_c} \tag{2}$$

where l_c is the length of the coil. When the coil resistance is known and R_L=R_c, the power output has the maximum value of

$$P_m = \frac{V_{oc}^2}{8R_c} = \frac{N^2\omega^2 A_e^2 \mu_{r,e}^2 B_{ex}^2}{8R_c} \tag{3}$$

The power output depends on various parameters as shown in (3). Theses parameters are not independent of each other. For instance, increasing B_{ex} by placing the MFEH closer to the rail track or increasing $\mu_{r,e}$ by optimising the magnetic core may also lead the increase of the coil resistance R_c; the increase of A_e may lead to a reduction in $\mu_{r,e}$. The complex relationships between these parameters have not been fully considered in previous studies and will be thoroughly investigated in this work to optimise the power generation.

The effective permeability $\mu_{r,e}$ is critical to the increase the power output. When a magnetic core with a finite length is magnetized by an external field, a demagnetization field opposing the external field is generated, leading to a decreased magnetic field in the magnetic core [24,32]. As a result, the effective permeability $\mu_{r,e}$ of a magnetic core with a finite length is always smaller than relative permeability μ_r of the core material. The demagnetization field is dominated by the geometry of the magnetic core. Therefore, the shape of the magnetic core can be optimised to increase $\mu_{r,e}$.

Furthermore, the current I_c generated in the coil produces a secondary magnetic field. The average flux density of this field in the middle cross-section of the magnetic rod can be expressed as [32]

$$B_s = \frac{\mu_{r,e} N I_c}{l_c} \tag{4}$$

B_s is superimposed to B_{oc}, forming the total flux density B in the magnetic core. The flux density B has to be evaluated since all ferromagnetic materials have a saturation limit. When the coil inductance is cancelled out by the compensating capacitor and $R_c + R_L \ll \omega L_c$, it can be proved (see the supplementary material) that the total magnetic flux density B in the middle of the magnetic core can be approximated by the secondary field B_s (see (5)), hence its relationship with the power output can be described by (6).

$$B \approx B_s = \frac{\mu_{r,e} N I_c}{l_c} = \frac{\mu_0 \mu_{r,e}^2 N^2 A_e \omega B_{ex}}{(R_c + R_L) l_c} \tag{5}$$

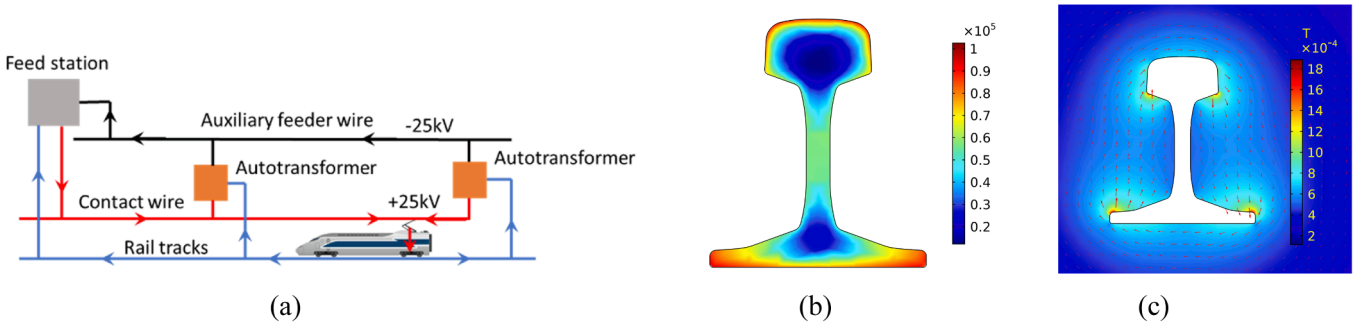

Fig. 1. (a) A schematic of the AC electric traction system based on auto-transformer; (b) the distribution of current in the rail track and (c) the magnetic flux density generated in its vicinity when the returning traction current is 300 A, 50 Hz. (b) and (c) are simulation results from COMSOL Multiphysics®.

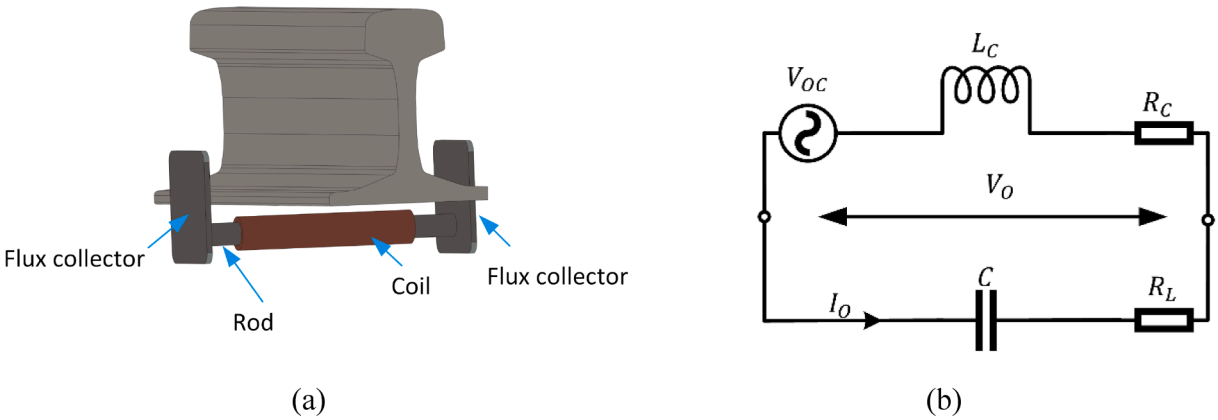

Fig. 2. Magnetic field energy harvesting: (a) a schematic of the magnetic field energy harvester and (b) an equivalent circuit model of the energy harvester connected to a load resistor and a compensating capacitor.

$$P = \frac{1}{2\mu_0}\cdot\frac{R_L}{R_c+R_L}\cdot A_c\omega l_c B_{ex}B_s \approx \frac{1}{2\mu_0}\cdot\frac{R_L}{R_c+R_L}\cdot A_c\omega l_c B_{ex}B \tag{6}$$

Since the flux density B_{ex}generated by the rail track decreases with the distance to the rail track (Fig. 1 (c)), it is desirable to place the MFEH close to the rail track to generate high power according to (3). However, when the MFEH is close to the rail track, the magnetic field generated by the MFEH produces circular eddy currents in the rail track, leading to an energy loss. This energy loss is reflected as the increased internal resistance of the coil, which can be expressed as

$$R_c = R_w + R_{ed} \tag{7}$$

where R_w is the wire resistance of the coil; R_{ed} is the increase of coil resistance due to the eddy current; R_w and R_{ed} can be further expressed as

$$R_w = \frac{(d_i + d_o)\pi N^2}{2\sigma_w A_w} \tag{8}$$

$$R_{ed} = \frac{2P_{ed}}{I_c^2} \tag{9}$$

where d_i and d_o are the inner and outer diameter of the coil; σ_w and A_w are the electrical conductivity and cross-section area of the coil wire; P_{ed} is the average power dissipation of the eddy current. In addition to increasing coil resistance, the eddy currents also affect the coil inductance through the generation of a magnetic field opposing the one generated by the magnetic core [33]. Therefore, the effects of the rail track on the MFEH have to be considered during the modelling and design.

3. Finite element modelling of the MFEH

To aid the design and optimisation, an electromagnetic-circuit-coupled finite element model was developed in COMSOL Multiphysics®. It includes the simulation of eddy current generation and can predict the full matrix performance of an MFEH connected to an electrical circuit. The 3D model, shown in Fig. 3, was placed in the centre of an air enclosure (not shown in the figure). The material of the rail track was assigned a relative permeability of 30 and electrical conductivity of 3×10^6 S/m, both of which are within the typical ranges reported in the literature [34,35]. The magnetic core material was modelled as MnZn ferrite, which has a very low electrical conductivity (~1 S/m) and high relative permeability. Its low electrical conductivity makes the eddy current losses in itself negligible. The relative permeability μ_r of the

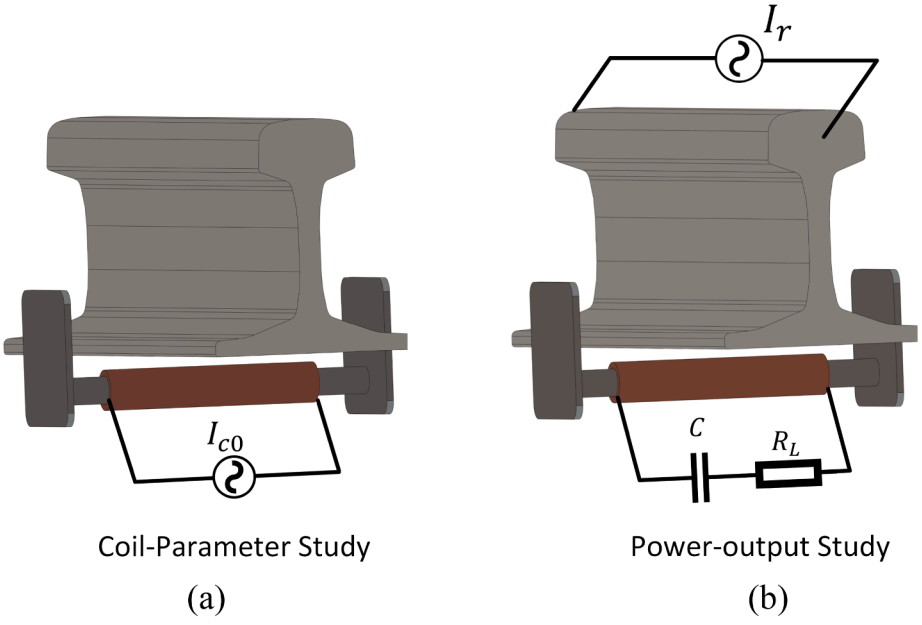

Fig. 3. A schematic of the finite element model of the magnetic field energy harvester: (a) the Coil-parameter Study and (b) the Power-output study.

magnetic core was assigned with various values to investigate its effect on the performance. A linear magnetization was assumed for the magnetic core, which means μ_r is independent of the magnetic field strength. Unless specified, the circular coil was wound by copper wires with a diameter of 0.2 mm and an electrical conductivity of 6×10^7 S/m. The diameter of the wire affects the voltage and current output of the MFEH but not the power output. Other parameters of the coil are optimised in Section 4, including the coil length and the number of windings.

The FEM consists of two studies: Coil-parameter Study to simulate the coil resistance and inductance, and Power-output Study to simulate the power output and flux density when the MFEH is connected to a circuit. Both studies are frequency domain analysis at 50 Hz. In the Coil-parameter study, the coil was energised by a current source with an amplitude of I_{c0}, as shown in Fig. 3 (a) while the rail track was open-circuited. I_{c0} generated a voltage V_{c0} cross the coil. The ratio of V_{co} to I_{c0} was the complex impedance of the coil, from which the coil resistance $R_c$and inductance L_c were identified. The model was built in the 'Magnetic and Electrical Interface' (MEI) of COMSOL. MEI can compute the magnetic field and eddy current distribution by applying Ampere's Law and Current Conservation [36]. As a result, the simulated L_c and R_c included the effects of the eddy current generated in the rail track.

In the Power-output Study, the rail track was energised with a current I_r of 300 A through the cross-sections at both ends, simulating the traction return current, as shown in Fig. 3 (b). The current-carrying rail track and the MFEH were modelled in the MEI to include the effects of eddy current generation. The output of the coil was connected to an 'Electrical Circuit Interface' (ECI), which has a compensating capacitor C and a load resistor R_L. R_L was set toR_c simulated in the Coil-parameter Study and C was calculated based on the simulated L_c by (2). The current I_c and magnetic field B_s generated by the coil depended on the voltage output simulated by in the MEI and the circuit in the ECI. The eddy current loss generated in the MEI also depended on B_s and therefore the circuit as well. In this way, the electromagnetic and electrical (circuit) domains of the MFEH are coupled together.

4. Design optimisation by finite element modelling

4.1. Shape of the magnetic core

Three designs of the magnetic core were considered for the MFEH, as shown in Fig. 4. Design 1 has a conventional rod-shaped core; Design 2 features two flux collectors being conformal to the profile of the rail; Design 3 has square flux collectors compared with Design 2. Both Design 2 and 3 partially encloses the rail tack and covers the rail foot. The three designs share the rod diameter$d = 20$ mm, rod length $l = 160$ mm, coil length$l_c = 100$ mm, the number of windings$N = 15{,}000$ and the diameter of coil wire$d_w = 0.2$ mm. The inner diameter $d_i$of the coil is the same as d. The flux collectors in Design 2 and 3 have the same height$h = 150$ mm, thickness$t = 5$ mm and depth$w = 100$ mm.

For each design, the open-circuit flux density B_{oc}in the middle of the rod is presented against the relative permeability $\mu_r$of the magnetic core material in Fig. 5 (a). When$\mu_r = 1$, i.e. the external magnetic field $B_{ex}$is not intensified, $B_{oc}$for all the three designs is 5.59×10^{-4} T. As μ_r increases, B_{oc} goes up. Both Design 2 and 3 show much higher B_{oc}than Design 1. When$\mu_r = 2000$, B_{oc} for Deign 1, 2 and 3 are 0.029, 0.21 and 0.17 T, respectively. The flux collectors guide more flux lines into the magnetic core, leading to higher flux density in Design 2 and 3 than Design 1. Alternatively, it can be explained as the reduction of the demagnetization factor $D$when the flux collectors are used [25]. The relationship between $\mu_{r,e}$ and Dcan be approximated as [37]

$$\mu_{r,e} \approx \frac{\mu_r}{1 + D(\mu_r - 1)} \tag{10}$$

(10) suggests that because of the demagnetization factor, $\mu_{r,e}$ is always smaller than μ_r when $\mu_r > 1$, which can be verified by the plot of $\mu_{r,e}$ against $\mu_r$presented in Fig. 5 (b). $\mu_{r,e}$ was calculated by the ratio of B_{oc} to B_{ex}. Moreover, when μ_r is sufficiently large, $\mu_{r,e}$ saturates at $1/D$, which in return leads to the saturation of B_{oc} in Fig. 5 (a). Clearly, Design 2 has the highest effective permeability among the three designs.

The coil inductance and the open-circuit voltage for all three designs follow the same trend as$\mu_{r,e}$, because they are linearly proportional to $\mu_{r,e}$ according to (1) and (2). The increase in R_c with μ_r, presented in Fig. 5 (e), is a result of the eddy current losses in the rail track. In the Coil-parameter simulation, where the coil is energised but the rail track is not, eddy currents are generated on the track, as shown in Fig. 6. Design 2 has the highest eddy current density covering the largest area, followed by Design 3 and Design 1. The simulated power loss P_{ed} and coil resistance R_c when$\mu_r = 2000$ are presented in Table 1. The power loss P_{ed} in the simulation was calculated as the volume integration of the electric loss density across the rail track [36]. Design 2 has the highest power loss, leading to the highest R_c. R_{ed} was calculated by (9) and compared with $R_c - R_w$ in Table 1, where R_w is 0.65 kΩ for all three designs. The good agreement between R_{ed} and $R_c - R_w$ validates (7) and (9).

The power output from each of the three designs saturates as μ_r increases, as shown in Fig. 5 (f). Both Design 2 and 3 show much higher power output than that from Design 1, validating the benefits of the flux collectors. When$\mu_r = 2000$, the power outputs of Design 1, 2 and 3 are 0.16, 0.92 and 1.30 W, respectively. Although Design 3 has a lower effective permeability, flux density and open-circuit voltage than Design 2, its power output is 41.3% higher because it induces a lower eddy current loss and thus has a lower internal resistance. Therefore, the higher effective permeability does not always lead to higher power output. The optimal design should trade off the effective permeability against the eddy current loss. Based on the power output, Design 3 was selected for the rest of this study for further study.

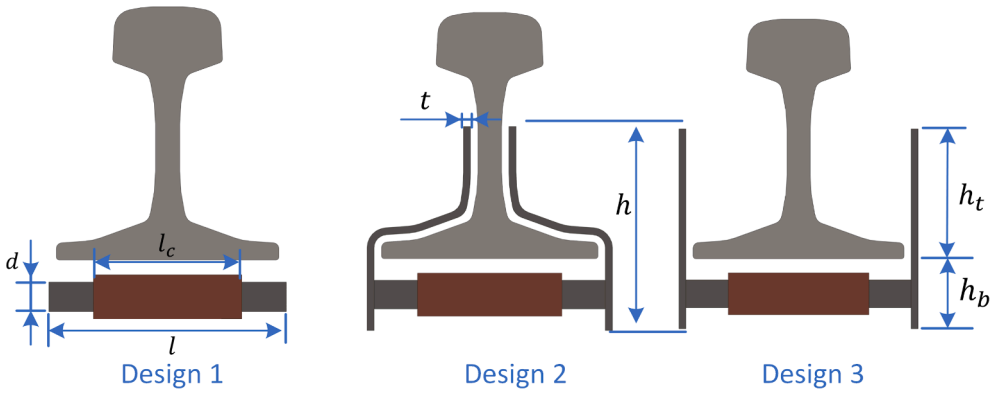

Fig. 4. Three designs of the magnetic field energy harvester with different magnetic cores.

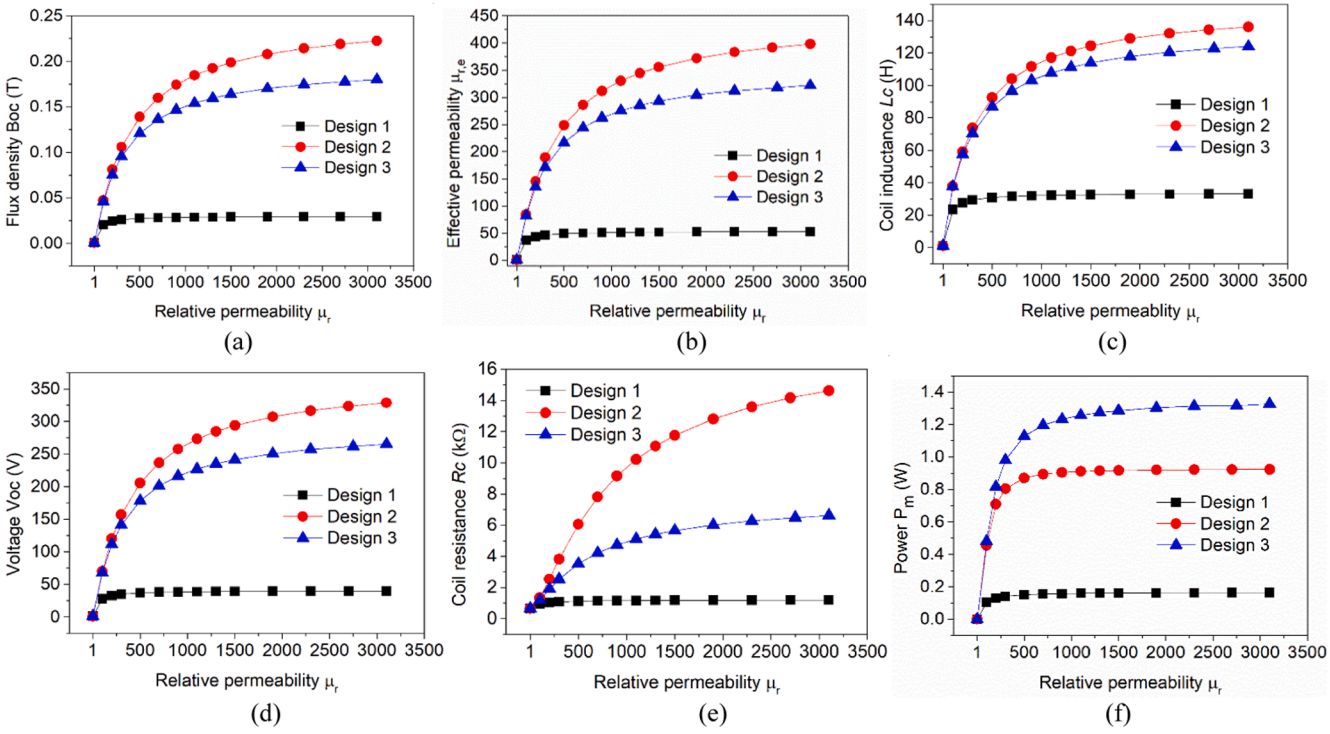

Fig. 5. Comparison of the performances of the three designs of the magnetic field energy harvester: (a) open-circuit flux density B_{oc}; (b) effective permeability $\mu_{r,e}$; (c) coil inductance L_c; (d) open-circuit voltage V_{oc}; (e) coil resistance R_c; (f) power output.

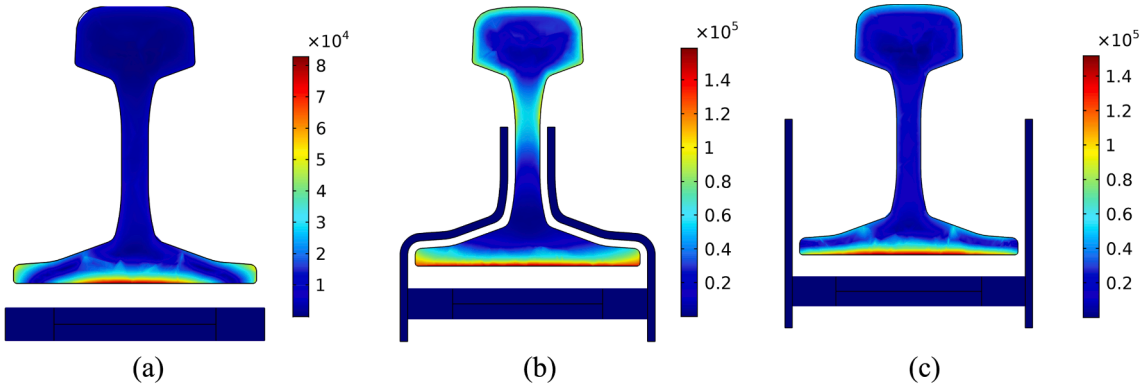

Fig. 6. Induced current density (unit A/m^2) in Coil-parameter study where the coil is energised withI_{c0} = 0.01 A and the track is not energised: (a) Design 1, (b) Design 2 and (c) Design 3.μ_r = 2000 was used for all three designs.

Table 1
Simulated coil losses in Coil-parameter study withI_{c0} = 0.01 A.

Parameters	Design 1	Design 2	Design 3
P_{ed}(W)	0.027	0.627	0.276
R_c(kΩ)	1.193	13.202	6.214
R_{ed}(kΩ)	0.540	12.540	5.528
$R_c - R_w$(kΩ)	0.543	12.552	5.564

4.2. Dimensions of the magnetic core

Following the optimisation on the shape of the magnetic core, simulations were performed on Design 3 withμ_r = 2000, l_c=100 mm and$N$ = 15000 to investigates the effects of the magnetic core's dimensions on the outputs. Fig. 7 shows the performance of the MFEH against the magnetic core length l. As l is increased from 150 mm to 1150 mm, the flux density B_{oc} and the voltage V_{oc} first decreases and then increases. When l increases, on one hand, the magnetic flux collectors are placed further away from the rail track and thus in a weaker magnetic field, leading to a reduced number of flux lines guided into the magnetic core and hence the decrease in B_{oc}. On the other hand, the demagnetization factor of a magnetic core generally gets smaller as the ratio of l/dincreases [38], leading to increased effective permeability. The coil resistance decreases progressively with l and then plateaus, as shown in Fig. 7 (b). This suggests that when the flux collectors are placed away from the rail track, a lower eddy current loss is produced. Due to the decrease of the coil resistance, the power generated increases monotonously with the magnetic core length. Therefore, a longer magnetic core is preferred for higher power generation.

The dimensions of the flux collectors affect the power output through both the open-circuit voltage and the coil resistance, similar to the core length. For the conciseness of the paper, only the effects of these parameters on the power output are presented in Fig. 8, which shows that the increase of the length l, height h and thickness w leads to an increase

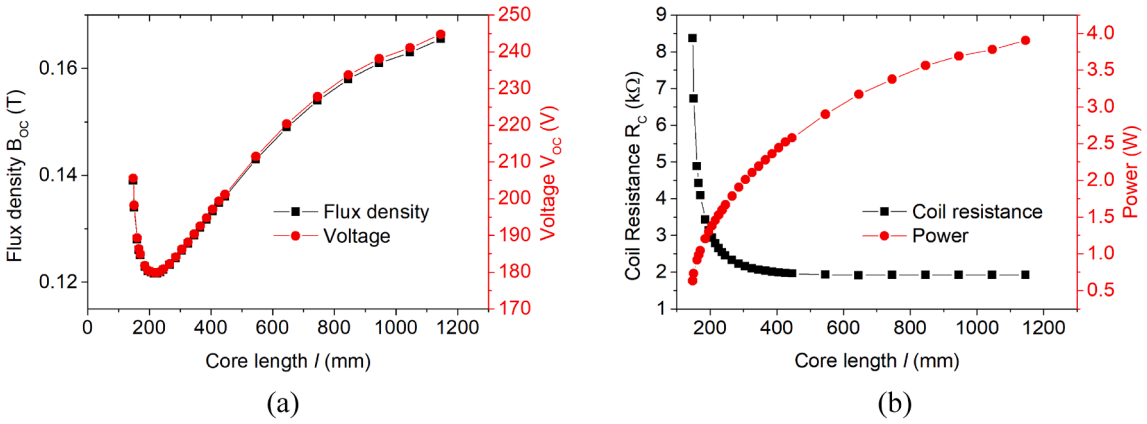

Fig. 7. Effects of the magnetic core length l on the performance of the MFEH: (a) coil inductance and open-circuit flux density and (b) coil resistance and power.

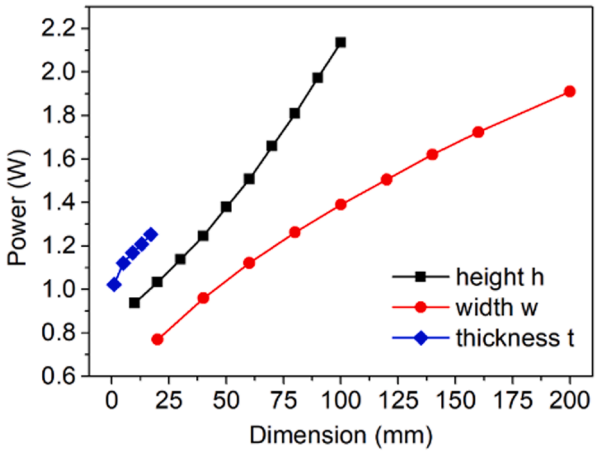

Fig. 8. Effects of the height, width and thickness of the flux collectors on the power output of the MFEH.

in the power output. Combining the results in Fig. 7 and Fig. 8, it can be concluded that the power output of the MFEH can be increased by increasing the length of the rod and the size of the flux collectors. Therefore, the optimal dimensions are the maximum permitted by practical constraints such as installation space, device weight, and cost. For the rest of the studies in Section 4, the values of l, h, w and t are selected as 210, 100, 100 and 5 mm, respectively.

4.3. Coil length

The effects of the coil length l_c on the performance of the MFEH are presented in Fig. 9. In all the cases, the number of windings N is kept constant at 10,000 by varying the outer diameter d_o by

$$N = \frac{l_c(d_o - d_i)}{2d_w^2} \tag{11}$$

The open-circuit flux density B_{oc} does not change with l_c because B_{oc} is only related to the magnetic core and external magnetic field. It does not depend on the coil geometry. Although N is constant, the open-circuit voltage decreases slightly with l_c because the flux density in the magnetic rod is not strictly uniform along its length—it is highest in the middle. With a smaller l_c, the coil is concentrated in the middle of the rod, leading to a higher EMF.

The power output is increased from 1.20 to 1.50 W because of the reduction of the coil resistance $R_c$from 1.63 to 1.18 kΩ. When l_c increases, the same number of windings requires a smaller d_o. This results in the decrease of the total wire length in the coil and thus the reduction in the wire resistance R_w according to (8). However, when l_c is increased from 50 to 200 mm, R_w is only reduced from 0.47 to 0.37 kΩ. Therefore, the reduction in $R_w$is not the main cause of the reduction in R_c. The dominating factor for the reduction in R_c is the eddy current losses. Fig. 10 shows the flux density and eddy current density in Coil-parameter studies where the coil is energised with$I_{c0} = 0.01$ A and the track is not. With the same coil current, the shorter coil produces a higher flux density covering a shorter distance in the rod core. As a result, the shorter coil induces a higher eddy current density on the track. The simulated power losses P_{ed} for$l_c = 50$, 100 and 200 mm are

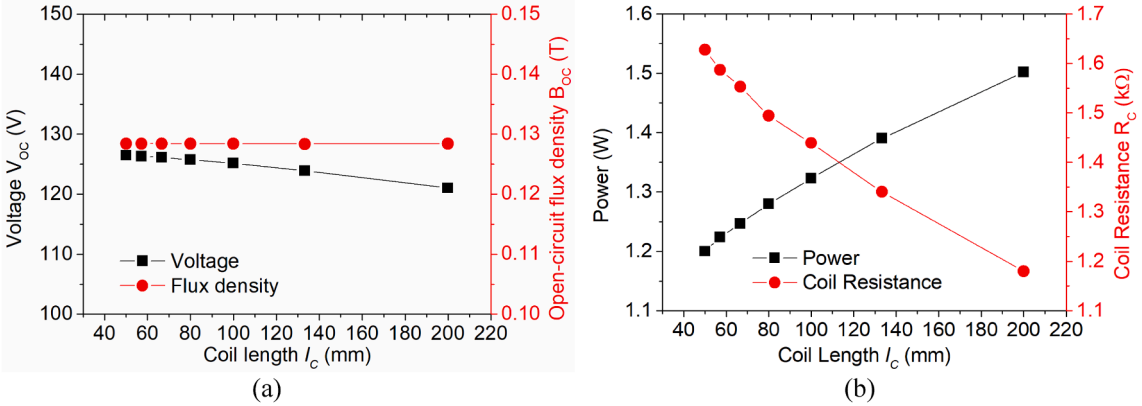

Fig. 9. Effect of the coil length l_c on (a) the open-circuit voltage and magnetic flux density and (b) the power output and coil resistance of the MFEH when the number of coil windings is fixed at 10,000.

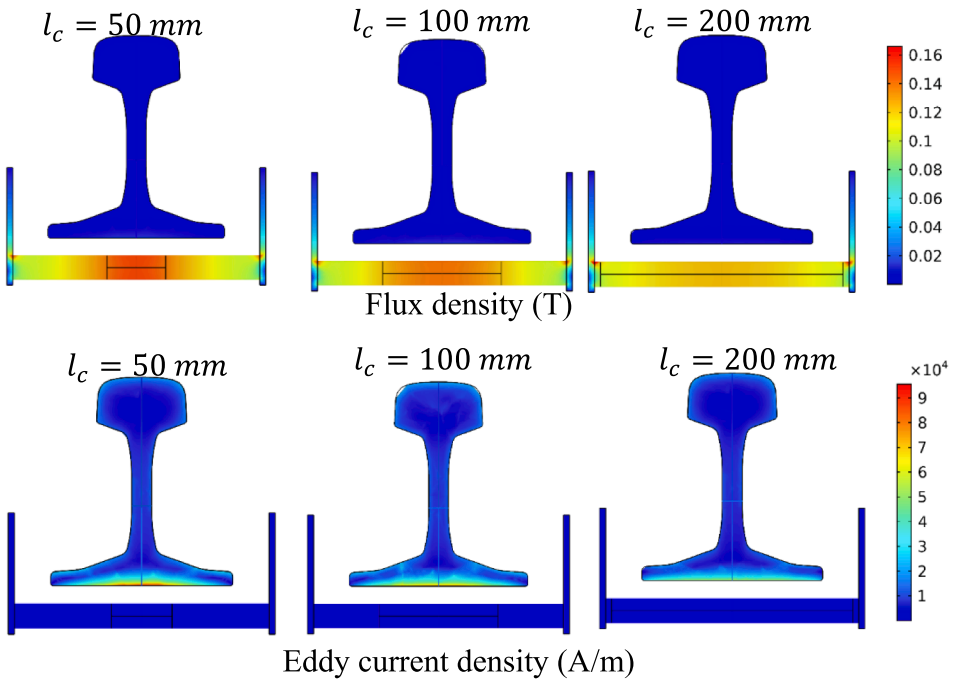

Fig. 10. Effects of the coil length l_c on the flux density and eddy current density in Coil-parameter study where the coil is energised with $I_{c0} = 0.01$ A and the track is not energised.

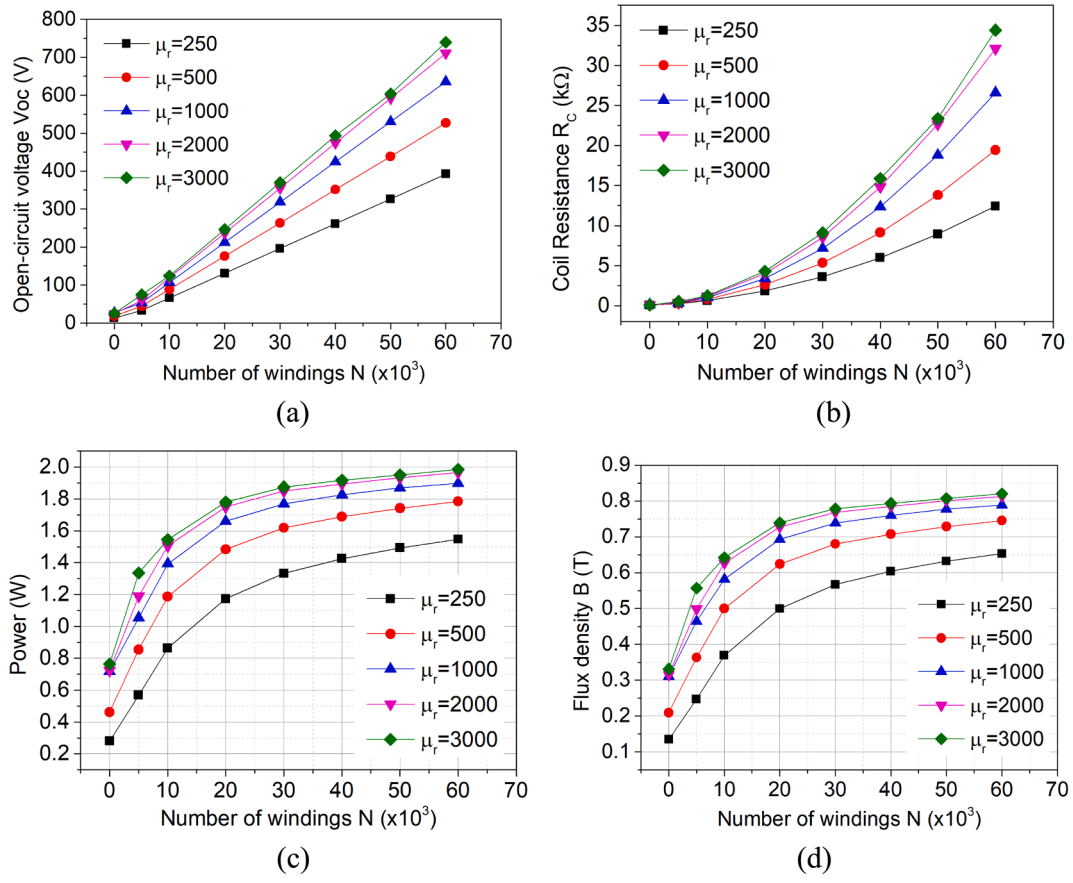

Fig. 11. Effects of the number of coil windings and relative permeability of the magnetic core on (a) the open-circuit voltage V_{oc}, (b) the coil resistance R_c, (c) the power output, and (d) flux density.*B*

0.054,0.052 and 0.038 W, respectively, resulting in R_{ed} of 1.55, 1.45 and 1.14 kΩ. Therefore, as l_c increases, the eddy current losses and R_{ed} decreases, giving rise to the reduction in R_c. Based on the results, the coil should always be wound as long as possible.

4.4. The number of coil windings

Fig. 11 shows the effects of the number of winding layers N_2 and the relative permeability μ_r of the magnetic core on the performance of the MFEH when l_c is fixed at 200 mm. The open-circuit voltage (Fig. 11 (a)) increases linearly with N, as expected according to (1). The coil resistance (Fig. 11 (b)) increases rapidly with N because of the increase in both the wire resistance and the eddy current losses. The power output (Fig. 11 (c)) first increases rapidly with N and then gradually flattens. When N is increased from 20 to 60, the maximum power is only increased from 1.8 to 2.0 W. This is because as more windings are added to the coil, the increased coil resistance gradually overshadows the increase of the open-circuit voltage, leading to little power increase eventually.

The variation pattern of V_{oc}, R_c and P with N are almost independent of μ_r. At each N, the values of V_{oc}, R_c and P eventually saturates with μ_r because of the saturation of the effective permeability, as discussed in Section 4.1. When$\mu_r > 2000$, the increase of μ_r hardly increases the power output. Based on the power output characteristics, the number of windings N is selected as 20,000 and the relative permeability of the magnetic core μ_r is selected as 2000.

4.5. Considerations on the flux density

The average flux density B in the middle cross-section of the magnetic core shows the same pattern as the power output, as shown in Fig. 11 (d). It must be noted that B is the total flux density combining the magnetic field generated by the rail current and the secondary field generated by the MFEH. Combining Fig. (c) and (d), it can be seen that the same power output can be achieved by different combinations of μ_r and N_2 but the resulted B is the same. For instance, a power output of 1.2 W can be obtained by three configurations: (a)$\mu_r = 2000$ and$N = 5000$; (b)$\mu_r = 500$ and$N = 10{,}000$; (c)$\mu_r = 250$ and$N = 30{,}000$. The values of B for the three configurations are the same as 0.5 T. This is because the coil inductance is cancelled out by the capacitor and the load resistance $R_L = R_c \ll \omega L_c$ in all cases. As a result, the ratio between P and B is independent of N and μ_r, according (6), which can be further verified by plotting the power in Fig. 11 (c) against the corresponding B in Fig. 11 (d), as presented in Fig. 12. There is a clear linear relationship between P and B, agreeing with (6).

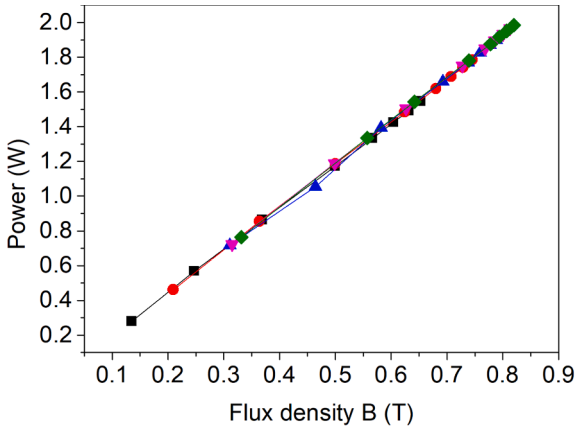

Fig. 12. The power output of the MFEH against the average flux density B in the middle of the magnetic core when the MFEH is connected to the optimal load resistance; B is the total flux density combining the external field generated by the rail current and the secondary filed generated by the MFEH.

With $N = 20{,}000$ and$\mu_r = 2000$, the flux density Bin the magnetic core is 0.7 T, which is higher than the usual magnetic saturation limit of MnZn ferrite (0.4–0.5 T). One way to reduce the flux density in the magnetic core is to increase the cross-section area $A_e$of the magnetic rod by increasing its diameter d. The effect of $A_e$on the performance of the MFEH is shown in Fig. 13. The open-circuit voltage V_{oc}increases with A_e but the relationship between V_{oc} and A_e is not linear as suggested by (1). This is because, as the diameter of the rod increases, its effective permeability μ_e decreases [38]. The increase in R_c is mainly due to the increased eddy current losses. As a result of the variation of V_{oc} and R_c, the power output slightly decreases with A_e. The flux density B decreases with A_e. After $A_e \geq 490$ mm^2 ($d \geq 25$ mm), the flux density in the magnetic core is less than 0.5 T. Therefore, the minimum magnetic rod diameter required for magnetic core is 25 mm.

5. Experiments and discussions

5.1. Device fabrication

Based on the design optimisation and the materials available, an MFEH was prototyped, as shown in Fig. 14 (a). The magnetic rod is made of MnZn ferrite PC40 ($d = 31.5$ mm and$l = 230$ mm) with initial permeability of 2300 and saturation limit of 0.51 T. The coil geometries selected in Section 4 were $N = 20{,}000$ with wire diameter$d_w = 0.2$ mm. To reduce the voltage output in the fabricated MFEH, the coil was designed with$N = 3200$ and$d_w = 0.5$ mm, which had the same coil volume as the coil with$N = 20{,}000$ and$d_w = 0.2$ mm. When the volume of the coil is constant, the reduction in the number of windings or the increase in the wire diameter reduces the voltage and increases the current generated, but it does not change the power output [39]. Due to the gaps between windings, the manufactured coil had 2798 windings. The outer diameter d_o and coil length l_c were 40 and 200 mm, respectively. The flux collectors are made of MnZn ferrite plate ($100 \times 100 \times 6$ mm^3, FPL100/100/6-BH1T, Kemet) with initial permeability of 3000 and a saturation limit of 0.52 T. The magnetic rod and plates were glued together by adhesive epoxy.

5.2. Experimental methods

During the experiments, the MFEH was placed underneath a section of rail track (1 m long), as shown in Fig. 14 (b). When measuring the coil resistance and inductance, the coil of the MFEH was connected to a Frequency Response Analyser (PSM1700, Newton 4th). The Frequency Response Analyser energised the coil with a voltage of 1 V peak-to-peak at 50 Hz and computed the coil resistance and inductance based on the measured voltage and current in the coil.

A combination of multilayer ceramic capacitors with capacitances of 0.1 and 1.2 μF was connected in series to the coil to cancel out the coil inductance. The combination of the capacitors was varied until the imaginary part of the total impedance of the coil and capacitors was minimised. Then a variable load resistance was connected in series to the capacitors and the coil. A current source (A5710-400–2 V0, VX Instruments GmbH) supplied 50 Hz AC to the rail track. The current amplitude in the rail track was monitored by a current probe (Pico Technology TA167). The voltage across the load resistor was measured to calculate the average power output.

5.3. Results and discussions

5.3.1. Coil resistance and inductance

The measured coil resistance $R_c$and inductance $L_c$of the fabricated device are compared with the simulation results in Table 2 with different conditions. '$d_c = \infty$' means the rail track was not present during the measurement; 'solenoid' refers to the magnetic rod with the coil but without the flux collectors; 'MFEH' refers to the fully assembled device. In the FEM, the MFEH and the coil were adjusted to the same as the

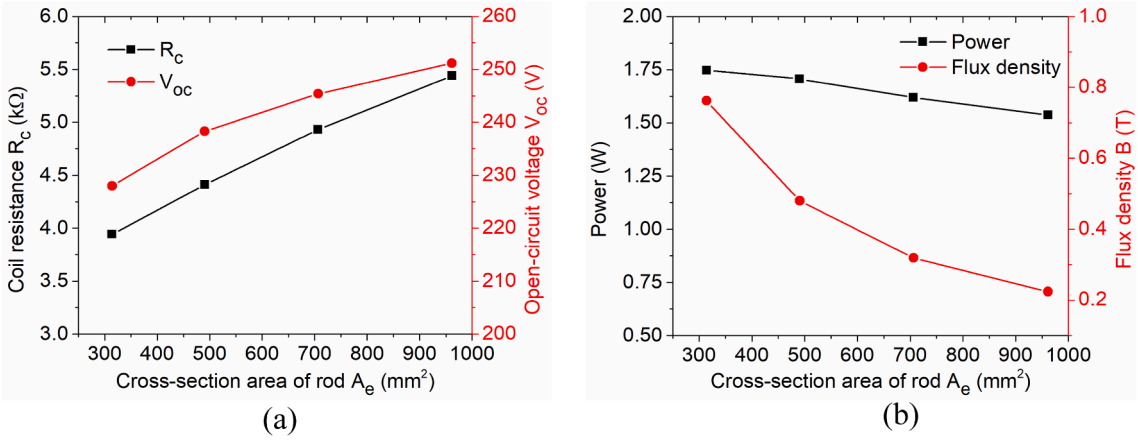

Fig. 13. Effects of the cross-section area of the magnetic rod on (a) the coil resistance R_c and open-circuit voltage V_{oc}; (b) the power output and flux density in the middle of the magnetic rod.

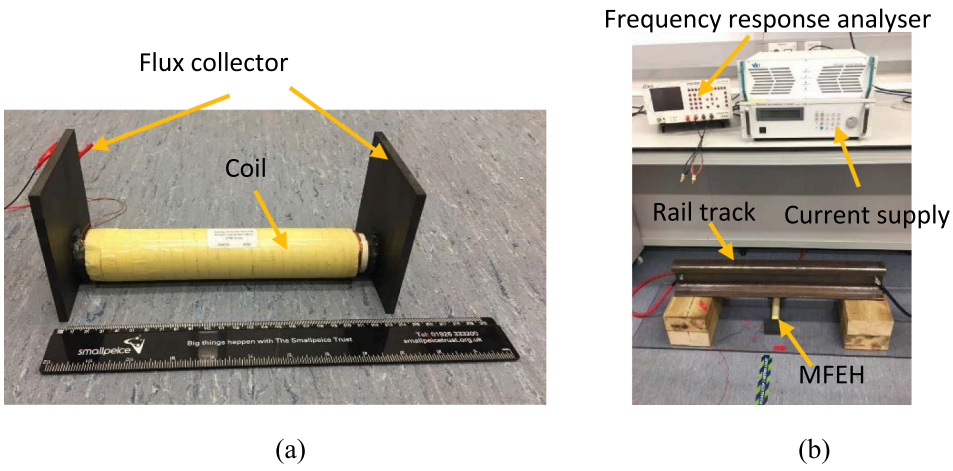

Fig. 14. (a) the prototyped MFEH and (b) the experimental setup.

Table 2
Comparison of measured and simulated coil parameters.

	R_c(Ω)		L_c(H)		C(μF)		Exp. final impedance (Ω)	
Conditions	Exp.	FEM	Exp.	FEM	Exp.	FEM	Resistance	Reactance
Solenoid$d_c = \infty$	27.2	26.9	1.19	1.19	–	–	–	–
MFEH$d_c = \infty$	27.7	27.1	2.64	2.80	–	–	–	–
MFEHd_c = 190 mm	31.2	31.4	2.67	2.82	3.79	3.58	34.9	0.89
MFEHd_c = 95 mm	46.5	50.7	2.78	2.97	3.61	3.42	49.87	0.76
MFEHd_c = 48 mm	71.2	77.8	2.89	3.09	3.49	3.29	77.1	3.10

prototyped.

The FEM predicts both R_c and L_c of the solenoid accurately. After the flux collectors are assembled, the simulated value of L_c is slightly higher than the measured, probably because of the gap introduced by the adhesive epoxy between the magnetic rod and flux collectors in the experiment. Overall, the simulated and measured coil parameters are in good agreement. Atd_c = 190 mm, R_c and L_c are about the same as when $d_c = \infty$, suggesting the negligible effects of the rail track and the eddy currents at this distance. As the MFEH is placed closer to the rail track, increases in both R_c and L_c are observed. The increase in R_c is resulted from the eddy current losses, as discussed in Section 4. The increase in L_c is a combined effect of the magnetic field generated by the eddy current and the reduction in the magnetic reluctance of the magnetic core resulted from the ferromagnetic rail track. A more detailed explanation and modelling of the effects of the ferromagnetic rail track can be found in [33]. Atd_c = 48 mm, the measured R_c is 71.2 Ω, which is 2.5 times of that at $d_c = \infty$, reflecting the importance of considering the eddy current losses for accurate modelling.

The capacitance used to tune out the coil inductance are also presented in Table 2. The final impedance is the impedance of the coil connected to the corresponding compensating capacitor. In the FEM, L_c could be tuned out accurately since an arbitrary capacitance can be specified. Therefore, the final impedance in the FEM is purely resistive with its resistance the same as R_c and is not presented. In the experiments, the accuracy of the tuning was limited by the capacitors available and as a result, the final impedance still has a small reactive part, as shown in Table 2. The resistance is increased slightly from R_c due to the resistive component of the capacitors.

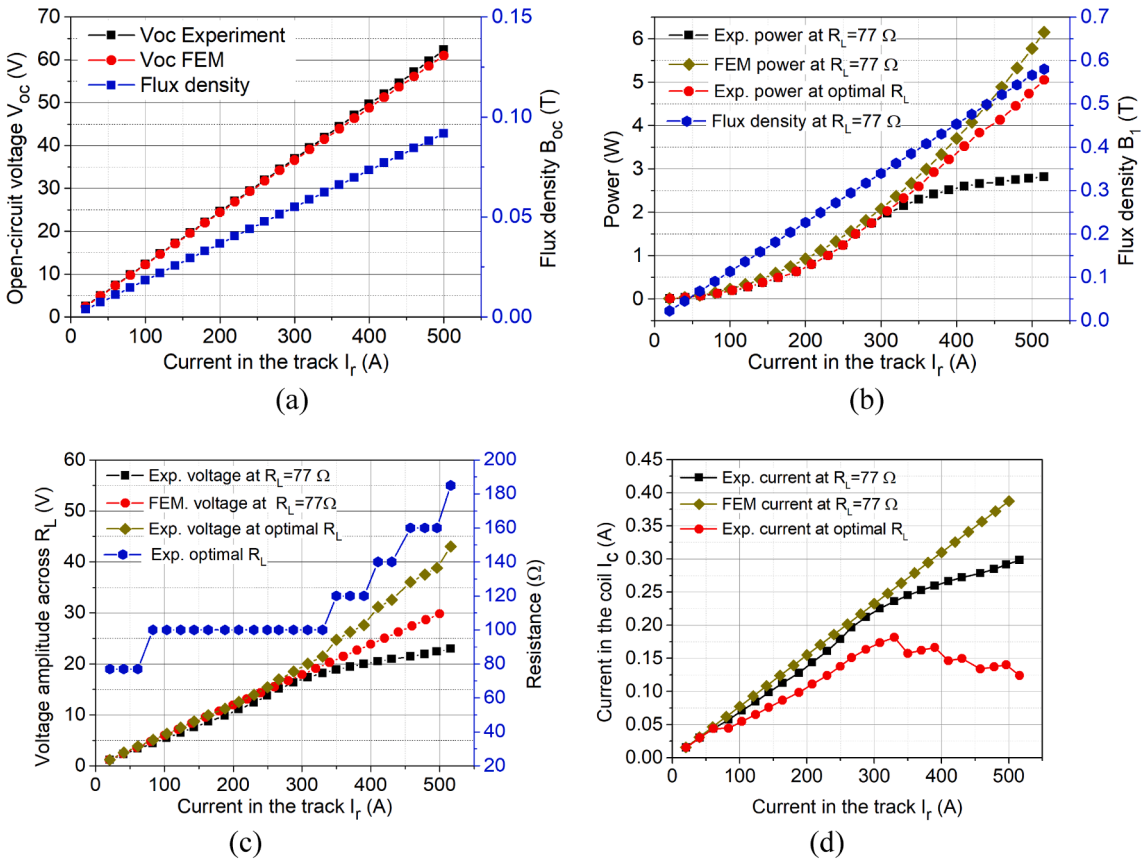

Fig. 15. Comparison of measured and simulated (a) open-circuit voltage V_{oc} and flux density B_{oc}; (b) average power and flux density B; (c) voltage amplitude across the load resistance; (d) current amplitude in the coil and through the load resistance.

5.3.2. *Power generation of the MFEH*

Atd_c = 48 mm, the measured open-circuit voltage V_{oc}agrees well with the simulated, as shown in Fig. 15 (a). V_{oc} increases linearly with the current $I_r$in the rail track. This is because the magnetic field generated by the rail track increases linearly with I_r, which can be verified by the linear relationship between B_{oc} and I_r.

The measured average power, zero-peak amplitudes of load voltage and current are compared with the simulation results in Fig. 15 (b-d). In the FEM, the load resistance $R_L$was kept constant at the coil resistanceR_c = 77 Ω since R_c is always the optimal load resistance. The simulated load voltage and current increases linearly with I_r and the simulated power increases proportionally to I_r^2, as expected. In the experiments, whenR_L = 77 Ω, the measured power first increases rapidly with I_r and then flattens gradually after I_r>~300 A. The flattening of the power is likely caused by the nonlinear magnetization and magnetic saturation of the magnetic core when the flux density is increased. The simulated average flux density B increases linearly with I_r, as shown in Fig. 15 (b). AtI_r = 300 A, B is as high as 0.35 T, leading to the nonlinear magnetization and hysteresis loss in the experiment. Moreover, high flux densities (>0.51 T) are concentrated in the corners, as shown in Fig. 16, leading to the magnetic saturation in those locations. The nonlinear magnetization and magnetic saturation in the experiment lead to a slower increase of the voltage amplitudes with I_r, as shown in Fig. 15 (c), and distortions in the voltage waveform, as shown in Fig. 17 (c). The slow increase in voltage amplitude and the distortions in the voltage waveform results in little power increase with I_r afterI_r > 300 A.

To fully test the power characteristics, at each value of I_r, the load resistance R_L in the experiments was varied until the optimal load resistance yielding the maximum power was obtained. The measured power with the optimal R_L is presented in Fig. 15 (a). The measured optimal load resistance (Fig. 15 (b)) was found to increase with the I_r.

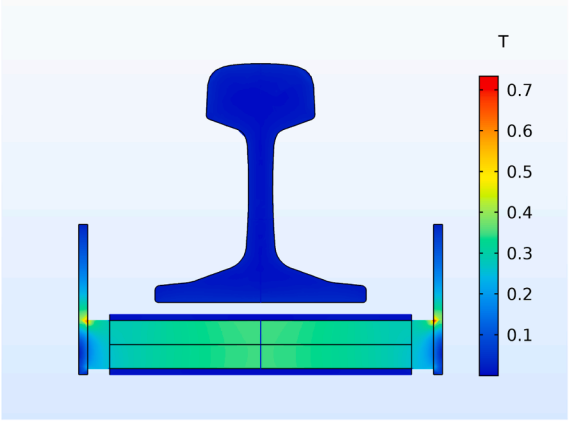

Fig. 16. Simulated flux density whenI_r = 300 A andR_L = 77 Ω. The average flux density in the middle of the magnetic core is 0.35 T but higher flux densities are observed in the corners.

WhenI_r = 100 A, the optimal load resistance is 100 Ω, instead of the coil resistance of 77 Ω, which can be verified by the power against R_L plot in Fig. 17 (a). WhenI_r = 520 A, the optimal load resistance is increased to 185 Ω (Fig. 17 (b)). The increase of the optimal load resistance is partly because of the increased loss, e.g. hysteresis loss, of the magnetic core as the flux density increases. It is also caused by the fact that the increase of the load resistance results in a reduced flux density, as suggested by (6). The flux density B in the magnetic core decreases monotonically with R_L, as shown in Fig. 17 (a) and (b). The reduction in the flux density reduces the negative effects of the high flux density, potentially leading to

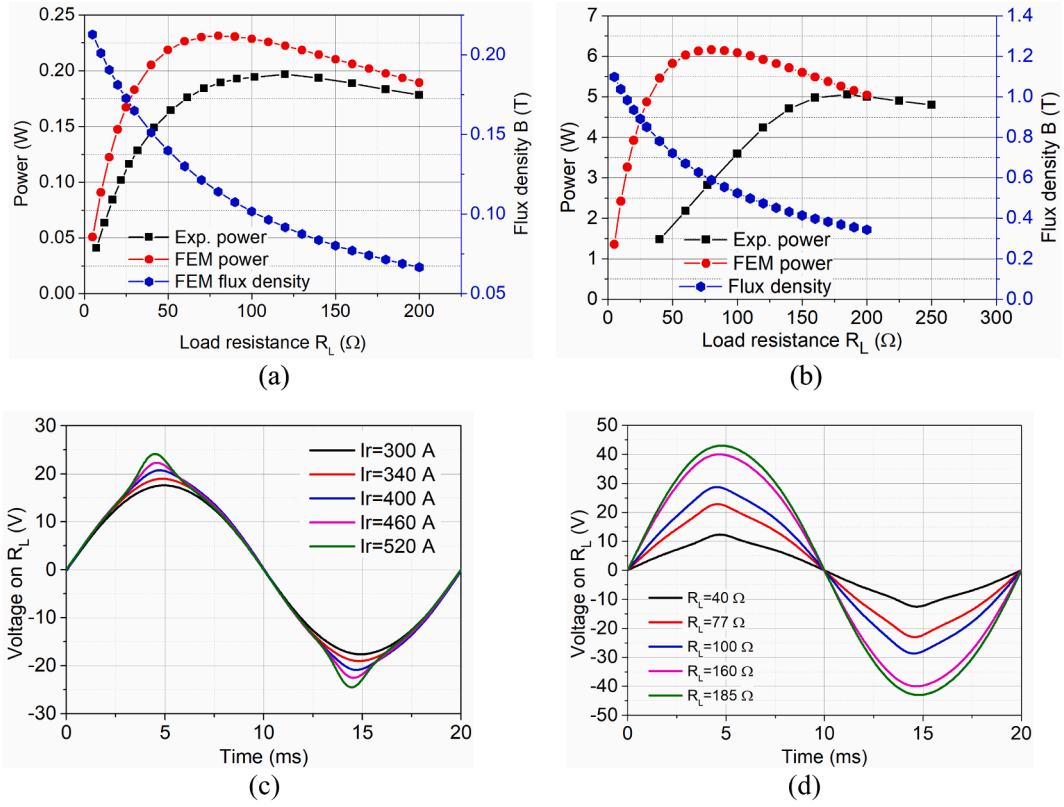

Fig. 17. Characteristics of MFEH withd_c = 48 mm: effects of the load resistance R_L on the power and flux density B when (a)I_r = 100 A and (b)I_r = 520 A; the dependence of the voltage across R_L on (c) I_r whenR_L = 77 Ω and (d) the load resistance R_L whenI_r = 520 A.

increased power output. This can be validated by the voltage measured on different load resistances when I_r is kept constant at 520 A, as presented in Fig. 17 (d). WhenR_L = 40 Ω, the measured load voltage is significantly distorted from a sinusoidal wave because of the magnetic saturation. The simulated flux density B (Fig. 17 (b)) in such a condition exceeds the saturation limit (0.51 T). As R_L increases, the distortions are gradually reduced, leading to an increase of power with R_L (Fig. 17 (b)). WhenR_L = 185 Ω, the distortion disappears and the maximum power of 5.05 W is produced. Despite the increased optimal load resistance, the measured maximum power is only 17.8% down from the simulated power of 6.15 W. This is with attributed to the slow decrease of the power R_L when R_L is increased beyond the optimal value.

As the distance d_c increases, the open-circuit voltage decreases, as shown in Fig. 18 (a), because the magnetic field generated by the rail track decreases with the distance to the rail track. The measured power output whend_c = 95 and 190 mm is compared with simulation in Fig. 18 (b-c). The characteristics of the measured power output are similar to that ofd_c = 48 mm. When the load resistance R_L equals to the coil resistance, the power output gradually flattens with I_r. A higher power output can be generated by increasing the load resistance beyond the coil resistance. AtI_r = 520 A, the maximum power measured in the experiment is 3.5 and 1.6 W ford_c = 95 and 190 mm, respectively, coprresponding to 69.3% and 31.7% of the power generated atd_c = 48 mm. Although the MFEH generates lower power with a larger d_c, the simulated flux density in the magnetic core is about the same for the three d_c, as can be seen from Fig. 15 (b) and Fig. 18 (b-c). The flux densities B ford_c = 48, 95 and 190 mm atI_r = 300 A are 0.34, 0.35 and 0.34 T, respectively. This explains that whend_c = 95 mm, the measured power withR_L = 50 Ω starts to flatten at about the same I_r (300 A) asd_c = 48 mm. The measured power whend_c = 190 mm starts to flatten at a higher value of I_r (~380 A) because the descrepacy between the measured and simulated power is larger than the other two distances.

The measured power outputs of the MFEH at different conditions are summarized in Table 3. The power consumption of sensors for railway

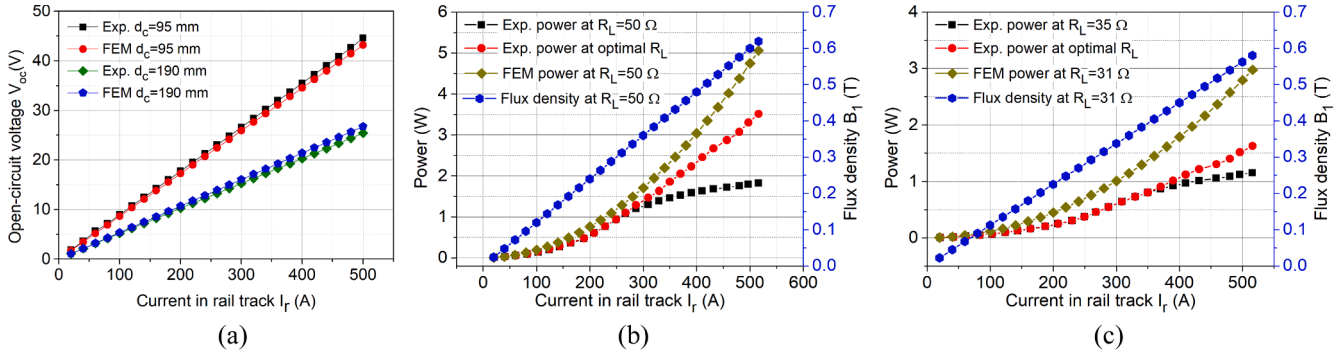

Fig. 18. Performance of the MFEH placed at different distances from the rail track: (a) the open-circuit voltage; the power output and flux density when (b)d_c = 95 mm (b) and (c)d_c = 190 mm.

Table 3
Measured power output of the MFET at different distance and rail current.

	Power at different rail current I_r (W)			
d_c(mm)	I_r = 100 A	I_r = 200 A	I_r = 300 A	I_r = 520 A
48	0.20	0.80	2.03	5.05
95	0.15	0.61	1.47	3.51
190	0.068	0.25	0.64	1.62

monitoring varies from hundreds of microwatts (e.g. MEMS accelerometer, infrared detector) to hundreds of milliwatts (strain gauge, pressure sensor) [40]. The power generated by the MFEH is sufficient to power those sensors to establish self-powered condition monitoring.

6. Conclusions

In this paper, a magnetic field energy harvester (MFEH) with multi-watts power was designed, optimised and tested for energy harvesting from the traction return currents in rail tracks. Based on the magnetic field distribution around the rail track, the magnetic core was designed with two flux collectors to partially enclose the rail track so that the high-strength magnetic fields around both corners of the rail foot could be used for power generation. The design and optimisation were carried out in electromagnetic-circuit coupled finite element model, which included the effects of the eddy current generation in the rail track. The design parameters investigated included the shape, dimensions and magnetic permeability of the magnetic core, the length and number of windings of the coil and the load-dependent flux density in the magnetic core. The flux collectors can increase the effective permeability by guiding more flux lines into the magnetic core and reducing the demagnetization effect, leading to an increased open-circuit voltage. However, the increase in the effective permeability also leads to increased eddy current loss in the rail track. The optimal design to maximise the power output should trade the effective permeability against the eddy current loss. Increasing the permeability $\mu_r$of the magnetic core material leads to increased power in the beginning but the effect gradually diminishes when μ_r is large enough because of the saturation of the effective permeability. The power output of the MFEH can be improved by increasing the length of the magnetic rod and the size of the flux collectors. The coil length should be as long as possible to reduce the coil resistance and increase the power output. When the total number of windings increases, the power output first increases rapidly and then gradually flattens due to the increased coil resistance resulted from the increased wire length and eddy current losses. The increase in the cross-section area of the magnetic rod reduces the flux density significantly while reducing the power slightly, and therefore can be used to prevent magnetic saturation.

The experimental results from the fabricated MFEH showed good agreement with the simulation results. An increase in the optimal load resistance was observed in the experiment because of the nonlinear magnetization and magnetic saturation of the magnetic core. This was also caused by the fact that the increase in the load resistance reduces the flux density and therefore reduce the negative effects of nonlinear magnetization and magnetic saturation, leading to an increase in power generation. Placing the MFEH further away from the rail track reduced the eddy current loss but also reduced the power output. When the MFEH was moved from a distance of 48 mm to 190 mm where the eddy current loss is negligible, the power output in the experiment was reduced from 5.05 to 1.6 W.

CRediT authorship contribution statement

Yang Kuang: Conceptualization, Methodology, Validation, Investigation, Formal analysis, Writing - original draft. **Zheng Jun Chew:** Investigation. **Tingwen Ruan:** Investigation. **Tim Lane:** Resources. **Ben Allen:** Resources. **Bimal Nayar:** Resources. **Meiling Zhu:** Supervision, Funding acquisition.

Declaration of Competing Interest

The authors declared that there is no conflict of interest.

Acknowledgement

The authors would like to acknowledge the support of the Engineering and Physical Science Research Council (EPSRC), UK through the grant 'Zero power, large area rail track monitoring' (EP/S024840/1).

References

[1] Hodge VJ, O'Keefe S, Weeks M, Moulds A. Wireless sensor networks for condition monitoring in the railway industry: A survey. IEEE Trans Intell Transp Syst 2014;16(3):1088–106.
[2] D.F. Transport. Transport statistics Great Britain 2018 [Online].
[3] Ngamkhanong C, Kaewunruen S, Costa BJA. State-of-the-art review of railway track resilience monitoring. Infrastructures 2018;3(1):3.
[4] Kuang Y, Hide R, Zhu M. Broadband energy harvesting by nonlinear magnetic rolling pendulum with subharmonic resonance. Appl Energy 2019/12/01/ 2019.; 255:113822.
[5] Bosso N, Magelli M, Zampieri N. Application of low-power energy harvesting solutions in the railway field: a review. Veh Syst Dyn 2020:1–31.
[6] Wang P, Wang Y, Gao M, Wang Y. Energy harvesting of track-borne transducers by train-induced wind. J Vibroengineering 2017;19(3):1624–40.
[7] Pan H, et al. A portable renewable wind energy harvesting system integrated S-rotor and H-rotor for self-powered applications in high-speed railway tunnels. Energy Convers Manage 2019;196:56–68.
[8] Cahill P, Nuallain NAN, Jackson N, Mathewson A, Karoumi R, Pakrashi V. Energy harvesting from train-induced response in bridges. J Bridge Eng 2014;19(9): 04014034.
[9] Wang J, Shi Z, Xiang H, Song G. Modeling on energy harvesting from a railway system using piezoelectric transducers. Smart Mater Struct 2015;24(10):105017.
[10] Gao M, Su C, Cong J, Yang F, Wang Y, Wang P. Harvesting thermoelectric energy from railway track. Energy 2019;180:315–29.
[11] M. Kroener, S. Ravindran, and P. Woias, "Variable reluctance harvester for applications in railroad monitoring," in Journal of Physics: Conference Series, 2013, vol. 476, no. 1, p. 012091: IOP Publishing.
[12] M. Kroener, N. Moll, S. Ravindran, P. Mehne, and P. Woias, "Characterization of a variable reluctance harvester," in Journal of Physics: Conference Series, 2014, vol. 557, no. 1, p. 012035: IOP Publishing.
[13] Zhang X, Pan H, Qi L, Zhang Z, Yuan Y, Liu Y. A renewable energy harvesting system using a mechanical vibration rectifier (MVR) for railroads. Appl Energy 2017;204:1535–43.
[14] Pourghodrat A, Nelson CA, Hansen SE, Kamarajugadda V, Platt SR. Power harvesting systems design for railroad safety. Proceedings of the Institution of Mechanical Engineers, Part F: Journal of Rail and Rapid Transit 2014;228(5): 504–21.
[15] Lin T, Wang JJ, Zuo L. Efficient electromagnetic energy harvester for railroad transportation. Mechatronics 2018;53:277–86.
[16] C. A. Nelson, A. Pourghodrat, and M. Fateh, "Energy harvesting from vertical deflection of railroad track using a hydraulic system for improving railroad track safety," in ASME 2011 International Mechanical Engineering Congress and Exposition, 2011, pp. 259-266: American Society of Mechanical Engineers.
[17] Lin T, Pan Y, Chen S, Zuo L. Modeling and field testing of an electromagnetic energy harvester for rail tracks with anchorless mounting. Appl Energy 2018;213: 219–26.
[18] Pan Y, et al. Modeling and field-test of a compact electromagnetic energy harvester for railroad transportation. Appl Energy 2019;247:309–21.
[19] Xing Z, Li J, Viehland D. Giant magnetoelectric effect in Pb (Zr, Ti) O 3-bimorph/NdFeB laminate device. Appl Phys Lett 2008;93(1):013505.
[20] Ryu J, et al. Ubiquitous magneto-mechano-electric generator. Energy Environ Sci 2015;8(8):2402–8.
[21] Roscoe NM, Judd MD. Harvesting energy from magnetic fields to power condition monitoring sensors. IEEE Sens J 2013;13(6):2263–70.
[22] Maharjan P, Salauddin M, Cho H, Park JY. An indoor power line based magnetic field energy harvester for self-powered wireless sensors in smart home applications. Appl Energy 2018;232:398–408.
[23] White R, Nguyen D-S, Wu Z, Wright P. Atmospheric Sensors and Energy Harvesters on Overhead Power Lines. Sensors 2018;18(1):114.
[24] Yuan S, Huang Y, Zhou J, Xu Q, Song C, Thompson P. Magnetic field energy harvesting under overhead power lines. IEEE Trans Power Electron 2015;30(11): 6191–202.
[25] Tashiro K, Wakiwaka H, Hattori G-Y. Estimation of effective permeability for dumbbell-shaped magnetic cores. IEEE Trans Magn 2015;51(1):1–4.
[26] Yuan S, Huang Y, Zhou J, Xu Q, Song C, Yuan G. A high-efficiency helical core for magnetic field energy harvesting. IEEE Trans Power Electron 2016;32(7):5365–76.
[27] S. Wright, M. Kiziroglou, S. Spasic, N. Radosevic, and E. Yeatman, "Inductive Energy Harvesting From Current-Carrying Structures," IEEE Sensors Letters, 2019.

[28] Oura Y, Mochinaga Y, Nagasawa H. Railway electric power feeding systems. Japan railway & transport review 1998;16(10):48–58.
[29] R. White, "AC/DC railway electrification and protection," 2012.
[30] F. Nyberg and R. Pollard. Network Rail A Guide to Overhead Electrification [Online]. Available: https://www.bathnes.gov.uk/sites/default/files/sitedocuments/Planning-and-Building-Control/Planning/nr_a_guide_to_overhead_electrification.pdf.
[31] Yang F, Du L, Chen W, Li J, Wang Y, Wang D. Hybrid energy harvesting for condition monitoring sensors in power grids. Energy 2017;118:435–45.
[32] Jiles D. Introduction to magnetism and magnetic materials. CRC Press; 2015.
[33] Y. Kuang, Z. J. Chew, T. Ruan, and Z. Meiling, "Magnetic field energy harvesting from current-carrying structures: electromagnetic-circuit-coupled model and experimental validation," IEEE Access, 2020.
[34] Dolara A, Leva S. Calculation of rail internal impedance by using finite elements methods and complex magnetic permeability. International Journal of Vehicular Technology 2009;2009.
[35] Mariscotti A, Pozzobon P. Resistance and internal inductance of traction rails at power frequency: A survey. IEEE Trans Veh Technol 2004;53(4):1069–75.
[36] C. Inc. COMSOL Documentation [Online]. Available: https://doc.comsol.com/5.5/docserver/#!/com.comsol.help.acdc/acdc_ug_magnetic_fields.08.087.html.
[37] Kaverine E, Palud S, Colombel F, Himdi M. Investigation on an effective magnetic permeability of the rod-shaped ferrites. Progress in electromagnetics research 2017;65:43–8.
[38] Paperno E, Grosz A. A miniature and ultralow power search coil optimized for a 20 mHz to 2 kHz frequency range. J Appl Phys 2009;105(7):07E708.
[39] Zuo L, Scully B, Shestani J, Zhou Y. Design and characterization of an electromagnetic energy harvester for vehicle suspensions. Smart Mater Struct 2010;19(4):045003.
[40] Gao M, Wang P, Wang Y, Yao L. Self-Powered ZigBee Wireless Sensor Nodes for Railway Condition Monitoring. IEEE Trans Intell Transp Syst 2018;19(3):900–9.